

Complete reconstruction of bound and unbound electronic wavefunctions in two-photon double ionization

P. A. Carpeggiani^{1,2,11}, E. V. Gryzlova^{3,11}, M. Reduzzi^{1,2}, A. Dubrouil¹, D. Faccialá^{1,2}, M. Negro^{1,2}, K. Ueda⁴, S. M. Burkov⁵, F. Frassetto⁶, F. Stienkemeier⁷, Y. Ovcharenko^{8,9}, M. Meyer⁹, O. Plekan¹⁰, P. Finetti¹⁰, K. C. Prince¹⁰, C. Callegari¹⁰, A. N. Grum-Grzhimailo^{3*} and G. Sansone^{7*}

To be complete, the characterization of the photoionization process of atoms and molecules requires the extraction of all quantum-mechanical phases and amplitudes. So far, complete experiments have accessed only the ionization process of neutral atoms and molecules. Here we report the quantum-mechanically complete characterization of the single and double ionization of neon to yield doubly charged ions. The first ionization step by intense, polarized extreme ultraviolet light from a free-electron laser leaves the ion in a polarized state (that is, one in which the angular momentum of the ion is aligned in space). By controlling the polarization of the light, we determine the bound and continuum components of the system in the first and second ionization steps leading to the formation of doubly charged neon ions. We test the validity of our approach by characterizing the influence of autoionizing ionic states on the two-photon double-ionization mechanism. Our results are important for understanding the physics of the interaction of extreme ultraviolet radiation with ions.

The interaction of vacuum and extreme ultraviolet (VUV–XUV) radiation with atoms and molecules is dominated by the photoionization process: a quantum of light is absorbed by the target and an electron is emitted. A great deal of physical insight into the electronic structure of the system and into the process of photoionization can be gained by analysing the properties of the emitted electrons (‘photoelectrons’).

Doubly or multiply charged ions can be created by the (sequential) absorption of several photons. The physics of their formation and the chemistry of their interactions are relevant for understanding processes in the interstellar medium¹ and in the outer parts of the ionosphere of the planets of the Solar System². The characterization of the electronic distribution of multiply charged ions could offer a new perspective for understanding the interactions with their environment (for example, in charge transfer processes in chemical reactions), with potential technological impact also for surface science³.

The advent of free-electron lasers (FELs) operating in the XUV and X-ray spectral range⁴ has opened new possibilities for the investigation of the formation of multiply charged ions in a laboratory environment^{5,6}. Due to the high intensity of FEL pulses, an initial target can absorb several XUV/X-ray photons, leading to the (sequential) emission of multiple photoelectron wavepackets. The three-dimensional photoelectron angular distribution (PAD) of the electron(s) released into the continuum is the result of the coherent superposition of several outgoing electron partial waves, characterized by different angular momenta. The complete description of the photoionization event calls for the characterization of all amplitudes and relative phases of these partial waves, whose number is

determined by the theoretical model used to describe the process. This complete information cannot be obtained, in general, by measuring only the PAD and cross-section, but additional observables are required^{7,8}. The quest for such a complete experiment, as the strongest test of theory and as a source of minimum information from which any observable can be predicted, was first formulated for electron–atom scattering at the end of the 1960s^{9,10}. Later, the concept of the complete experiment was extended to atomic photoionization^{11–15}, molecular photoionization^{16–18} and atomic Auger decay^{19–22} and played a crucial role in the progress of the physics of elementary atomic processes over decades^{23,24}. All of the complete experiments on photoionization so far have been performed with neutral targets.

The high intensity of FEL pulses, combined with the control of the polarization state of the XUV radiation²⁵, offers a new approach for accessing the electronic distribution in an ion after a photoionization event and, more generally, for performing a complete characterization of the photoionization event. The idea relies on the observation that atomic photoionization with polarized light leads to a residual ion^{26–28} in which the angular momentum is spatially aligned to a greater or lesser extent²⁹. The ion in this state is said to be polarized and this property can be exploited to derive the electronic distribution of the ion, by measuring the characteristics of the outgoing electrons in the first and second photoionization steps for different polarizations of the incident light. For this purpose multiphoton absorption, and therefore high intensities, are required for the experimental implementation of this scheme.

In this work we report the first complete characterization of all components (bound and unbound) of the complex electronic

¹Dipartimento di Fisica, Politecnico di Milano, Milan, Italy. ²IFN-CNR Politecnico, Milan, Italy. ³Skobeltsyn Institute of Nuclear Physics, Lomonosov Moscow State University, Moscow, Russia. ⁴Institute of Multidisciplinary Research for Advanced Materials, Tohoku University, Sendai, Japan. ⁵Pacific National University, Khabarovsk, Russia. ⁶IFN-CNR, Padua, Italy. ⁷Physikalisches Institut, Albert-Ludwigs-Universität Freiburg, Freiburg, Germany. ⁸Institut für Optik und Atomare Physik, TU Berlin, Berlin, Germany. ⁹European XFEL, Schenefeld, Germany. ¹⁰Elettra-Sincrotrone Trieste, Basovizza, Trieste, Italy. ¹¹These authors contributed equally: P. A. Carpeggiani, E. V. Gryzlova *e-mail: grum@sinp.msu.ru; giuseppe.sansone@physik.uni-freiburg.de

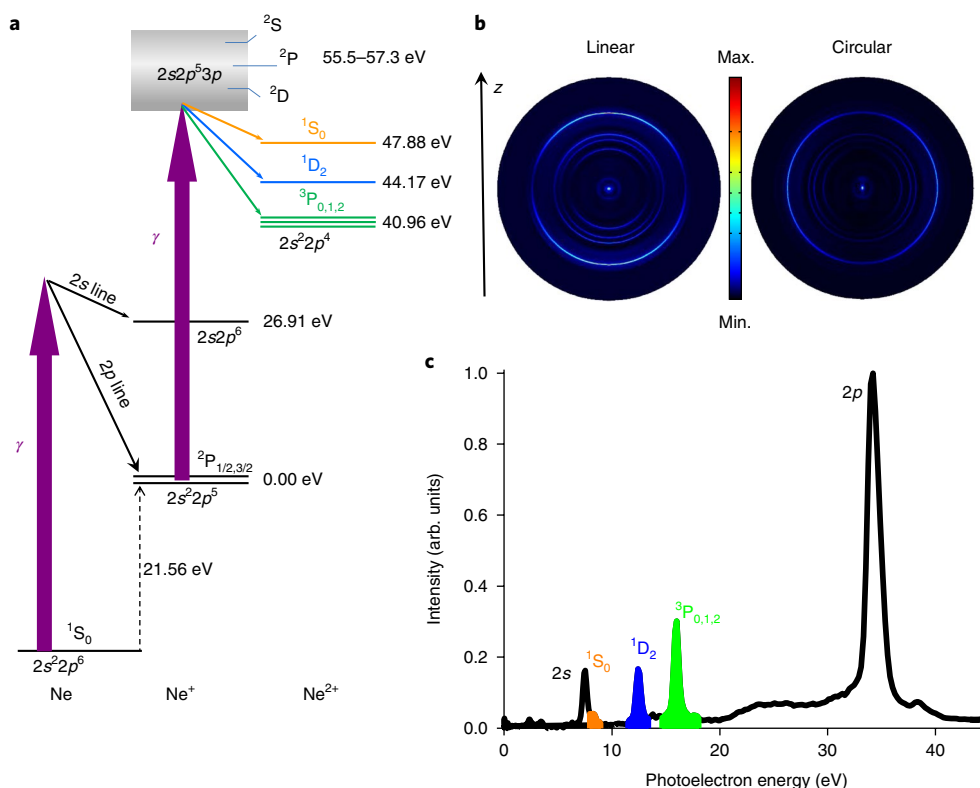


Fig. 1 | Energy-level diagram and photoelectron spectrum for the two-photon double ionization of neon. **a**, Energy-level scheme for singly and doubly ionized neon. The three final ionic states for doubly ionized neon $Ne^{2+} \ ^3P_{0,1,2}$, 1D_2 and 1S_0 are indicated by green, blue and orange lines, respectively (see Supplementary Table 2 for the energy values). In the photon energy range around 56.5 eV, the series of autoionizing states $2s2p^5 3p$ can be excited by single-photon absorption from the Ne^+ ground state. **b**, Inverted VMIS images for linear and circular polarizations. **c**, Photoelectron energy spectrum for linear polarization of the XUV pulses at a photon energy $\hbar\omega = 56.36$ eV.

wavepackets created in the process of two-photon double ionization in neon, for the first ($Ne + \gamma \rightarrow Ne^+ + e_1$) and second ($Ne^+ + \gamma \rightarrow Ne^{2+} + e_2$) ionization step. The simultaneous characterization of the outgoing electronic wavepacket and of the electronic distribution of the ion represents the most complete set of information that can be gained on the ion formation mechanism. We further validate our approach by characterizing the differences induced by an electronic resonance (an autoionizing state) on the electronic distribution of the ion.

Experiment

Our experimental approach is based on the measurement of the photoelectron yields and PADs generated by intense XUV femtosecond pulses with linear and circular polarization. By employing advanced theoretical analysis, this allows the extraction of the relative amplitudes and phases of the outgoing photoelectron waves for each ionization step, thus constituting a complete experiment.

The intense XUV pulses were delivered by the FEL FERMI operating at Elettra³⁰. The photoelectron spectra were acquired using the velocity map imaging spectrometer (VMIS) installed on the low-density matter experimental beamline³¹ (see Supplementary Information for a detailed description of the experimental parameters). The VMIS measures the momentum distribution of the outgoing electrons, from which both the angle-integrated spectrum (intensity versus energy) and the PAD at each energy can be extracted. Photoionization of $Ne^+(2s^2 2p^5 \ ^2P_{1/2,3/2})$ leads to doubly ionized neon with five different final ionic states ($2s^2 2p^4 \ ^3P_{0,1,2}$, 1D_2 , 1S_0), as shown in Fig. 1a. In the spectral range around 55.6 eV, the ionization spectrum of Ne^+ is characterized by a series of autoionizing states (shown in the dashed area) with the leading configuration

$2s2p^5 3p$ (ref.³²). These states decay to the above-mentioned five states of Ne^{2+} . The predicted energies of the autoionizing resonances are presented in the Supplementary Information. The VMIS images for linear and circular polarization are presented in Fig. 1b. The corresponding typical photoelectron spectrum acquired for linear polarization is shown in Fig. 1c. The photoelectron spectrum for circular polarization presents similar features. The $2p$ and $2s$ peaks correspond to the first ionization step from the $2p$ and $2s$ shells, respectively, while the 3P , 1D and 1S peaks indicate photoelectrons emitted in the second ionization step and resulting in the corresponding final ionic state. The 1S photoelectron peak partially overlaps with the photoelectrons emitted from the $2s$ shell in the first step, which limits the amount of information available for the 1S ionization channel.

Due to the two-photon nature of the process, within the dipole approximation the PADs for the lowest-order perturbation theory and for pulses containing many cycles are described by the relation³³:

$$I^\nu(\theta) = \frac{I_0^\nu}{4\pi} [1 + \beta_2^\nu P_2(\cos\theta) + \beta_4^\nu P_4(\cos\theta)] \quad (1)$$

where $P_n(x)$ is the n th Legendre polynomial, θ is the angle between the axis of symmetry z and the emission direction of the photoelectron, and I_0^ν is the angle-integrated intensity. In the cases of linearly ($\nu = L$) and of circularly ($\nu = C$) polarized pulses, the axis of symmetry z corresponds to the polarization direction and to the propagation direction of the XUV pulses, respectively (see Supplementary Fig. 1). Such a choice of the quantization z axis provides the simplest selection rules for the magnetic quantum numbers within the

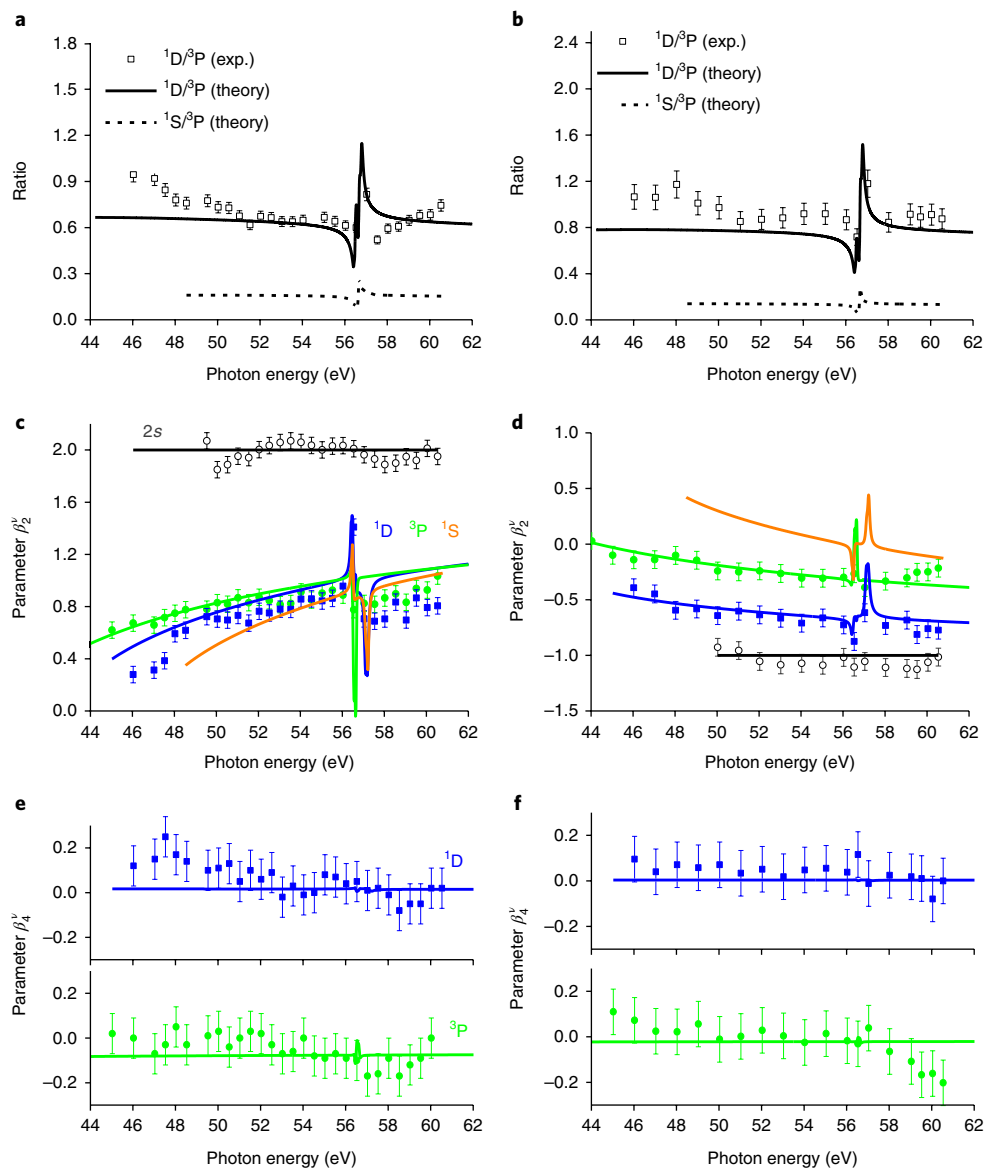


Fig. 2 | Two-photon double ionization of neon in the spectral range 44.0–62.0 eV. **a–f**, Experimental results (symbols) and theoretical simulations (lines) for linear (**a,c,e**) and circular (**b,d,f**) polarization. **a,b**, Ratio between the integral of the photoelectron peaks ^1D and ^3P , ^1S and ^3P . **c,d**, β_2^ν parameter for the ^1S (orange), ^1D (blue), ^3P (green) and $2s$ (black) photoelectron peaks. **e,f**, β_4^ν parameter for the ^1D (blue) and ^3P (green) photoelectron peaks. The error bars for β_2^ν and β_4^ν were calculated as the standard deviation of the data points for the $2s$ peak, and they were extended to the parameters of the other photoelectron peaks, as they show similar features on the VMIS images. The same approach was adopted for the error bars of the peak intensities.

electric dipole approximation³⁴. The parameters β_2^ν and β_4^ν are expressed in terms of the photoionization amplitudes for the intermediate ion and its polarization parameters before the second ionization step. The coefficient β_4^ν vanishes for the unpolarized intermediate ion.

The quality of the VMIS data allows the reliable determination of the branching ratio of the ^1S , ^1D and ^3P peaks and of the corresponding β_2^ν and β_4^ν parameters, which are shown in Fig. 2 for linear (left column) and circular (right column) polarizations of the XUV pulses. The β_2^ν and β_4^ν measured for the $2s$ line are in good agreement with the theoretical predictions $\beta_2^L = 2$, $\beta_2^C = -1$ and $\beta_4^{L,C} = 0$ (see Supplementary Information).

For the ^1D and ^3P peaks, the parameters β_4^ν do not vary much in this spectral range. The average values $\beta_4^L(^1\text{D}) = 0.06 \pm 0.09$ and $\beta_4^L(^3\text{P}) = 0.04 \pm 0.09$, and $\beta_4^C(^1\text{D}) = 0.04 \pm 0.1$ and $\beta_4^C(^3\text{P}) = -0.01 \pm 0.1$ indicate a possible small alignment of the intermediate ionic state (see Supplementary Information).

Theoretical model and comparison with the experiment

Our theoretical model considers a two-step process, in which the first ionization step leads to polarized intermediate ionic states $\text{Ne}^+(^2\text{P}_{1/2,3/2})$, and, in the second ionization step, the ion is further ionized by a second photon with the same frequency and polarization, leading to the emission of the second electron. The energies of the autoionizing states and all relevant transition matrix elements were obtained within the multiconfiguration Hartree–Fock approach (see Supplementary Table 3). In accordance with the pulse duration of FERMI (~ 50 fs), excitation of the intermediate fine-structure states $\text{Ne}^+(^2\text{P}_{1/2,3/2})$ is considered as incoherent^{35,36} (other details of the model are presented in the Supplementary Information).

The simulations are compared with the experimental data in Fig. 2. In general the simulations for linear and circular polarization are in close agreement with the experimental data for the parameters β_2^ν and β_4^ν , and with the ratio of the intensities of the photoelectron peaks, although some discrepancies can be observed in their

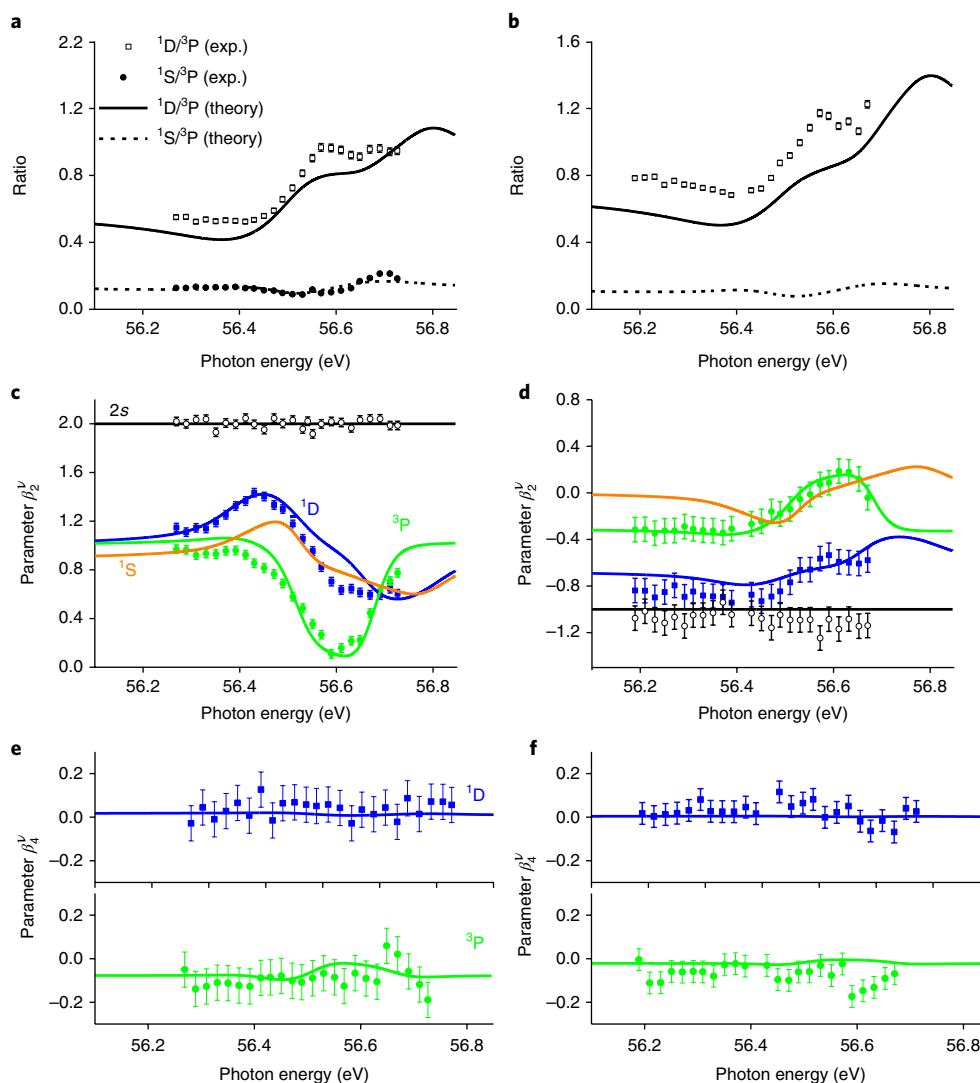


Fig. 3 | Two-photon double ionization of neon in the region of autoionizing states $2s2p^53p$. **a–f**, Experimental results (symbols) and theoretical simulations (lines) for linear (**a,c,e**) and circular (**b,d,f**) polarization. **a,b**, Ratio between the integral of the photoelectron peaks 1D and 3P , 1S and 3P . **c,d**, β_2^v parameter for the 1S (orange), 1D (blue), 3P (green) and $2s$ (black) photoelectron peaks. **e,f**, β_4^v parameter for the 1D (blue) and 3P (green) photoelectron peaks. The error bars for β_2^v and β_4^v were calculated as the standard deviation of the data points for the $2s$ peak, and they were extended to the parameters of the other photoelectron peaks, as they show similar features on the VMIS images. The same approach was adopted for the error bars of the peak intensities.

evolution as a function of the photon energy. In particular, the discrepancies between theory and experiment in Fig. 2a–c at low photon energies can be explained by the influence of Rydberg autoionizing ionic states $2p^4\ ^1S\ nl$, converging to the 1S threshold at 47.9 eV^{32,37,38}, which are not taken into account in our simulations. Furthermore, a dense set of two-particle atomic autoionizing states $Ne\ 2p^4\ ^3pnl$ is located below 52.7 eV^{39,40} and can indirectly influence the PAD of the second electron via polarization of the ion Ne^+ . Our experimental value of β_2^L in the energy range 58–61 eV (Fig. 2c) is lower than both, measured in ref.⁴¹ and calculated theoretically; this discrepancy could be related to the different coherence properties of the FEL in this spectral range, due to a change in the chirp of the seeding pulse.

The sharp feature around 56.5 eV corresponds to the region of the autoionizing resonances $Ne^+ 2s2p^53p$. The picture of multiple sequential photoionization steps based on an independent electron model fails to describe those aspects of the process that are strongly influenced by electronic correlation. The presence of metastable bound states embedded in the continuum (autoionizing states) strongly

influences the ionization probability and the PADs. To resolve this feature, we focused on the spectral range 56.1–56.8 eV, as shown in Fig. 3. The branching ratio between the different final ionic states 1S , 1D and 3P changes strongly in this region, indicating the influence of the dominant autoionizing resonance around 56.55 eV, which determines a twofold increase of the $^1D/^3P$ ratio for the linear polarization (Fig. 3a). A similar increase is visible also for circularly polarized pulses (Fig. 3b). The interference effect between the direct and indirect photoionization channels is clearly visible in the evolution of the $\beta_2^{L,C}$ parameters as shown in Fig. 3c,d.

The overall evolution well matches the theoretical calculations for both the 1D and 3P final ionic states. The good agreement is confirmed for linear and circular polarization. The parameters $\beta_4^{L,C}$ (Fig. 3e,f) do not show clear sharp resonances in this spectral region. The average values of these parameters are $\beta_4^{L,C}(^1D) = 0.04 \pm 0.04$, $\beta_4^{L,C}(^3P) = -0.09 \pm 0.05$, $\beta_4^C(^1D) = 0.02 \pm 0.04$ and $\beta_4^C(^3P) = -0.07 \pm 0.04$, in accordance with the theoretical predictions.

The good agreement between the simulated branching ratio and the β -parameters allows one to conclude that the perturbative

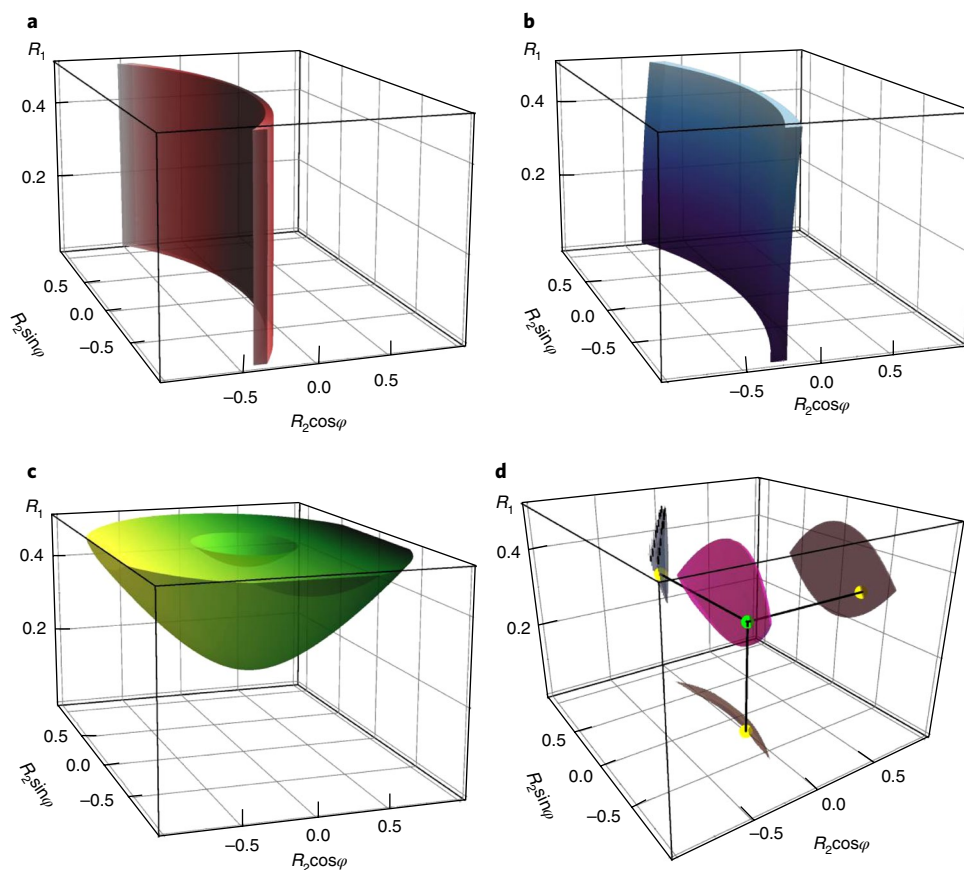


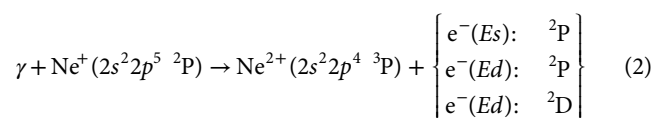
Fig. 4 | Complete experiment on photoionization of $\text{Ne}^+ 2p^5 2P$ to the $\text{Ne}^{2+} 2p^4 3P$ state at the photon energy 53 eV. a–c, Allowed sets of the quantum-mechanical parameters R_1 , $R_2 \cos \varphi$ and $R_2 \sin \varphi$ extracted from the experimental values of $\beta_2^L(3P)$ (red) (a), $\beta_2^C(3P)$ (blue) (b) and $\beta_4^L(3P)$ (green) (c). **d,** Finite volume (magenta) of the intersection of the sets from a–c, and result of the simulations (green dot) represented in the $\{R_1, R_2 \cos \varphi, R_2 \sin \varphi\}$ space. For a better visualization, the projections on the two-parameter planes are also displayed, for the volume of the intersections (brown surfaces) and for the result of the simulations (yellow dots).

approach in combination with the two-step ansatz can be used to describe the PADs for the linear and circular polarization in terms of the matrix elements of the ionization transitions in the first and second photoionization steps.

Reconstruction for the non-resonant case

We can use our theoretical model to derive the complete set of information about the electronic wavefunctions and realize the complete characterization of the outgoing wavepacket and of the electronic distribution of the residual ion for the first and second photoionization step of the $2p$ subshell. We first consider the photon energy interval 51–55 eV with a smooth (free of resonances) continuum. In a first approximation, the influence of the spin–orbit interaction on the electron wavefunctions can be neglected in this energy interval, as well as the configuration mixing. Thus, we can use the Cooper–Zare model of photoionization^{42,43}, where the dynamics of each photoionization step is described by three real quantities: two absolute values of the single-electron $2p$ - Es and $2p$ - Ed ionization amplitudes, $d_l^{(j)} = |d_l^{(j)}| \exp(i\varphi_l^{(j)})$ (the superscript $j = 1, 2$ indicates the step number, E stands for the photoelectron energy, $l = s, d$), and their relative phases $\varphi^{(j)} = \varphi_s^{(j)} - \varphi_d^{(j)}$. The polarization of the intermediate Ne^+ ion is described by only one real parameter, the absolute ratio $R_1 = |d_s^{(1)}| / |d_d^{(1)}|$. The dynamics of each step is defined by two parameters: $R_j = |d_s^{(j)}| / |d_d^{(j)}|$ and $\varphi^{(j)}$. The ratios R_1 and R_2 and phase $\varphi \equiv \varphi^{(2)}$ can be linked to the experimental data β_2^L , β_2^C , β_4^L and β_4^C (see Supplementary equations (1)–(4) and (7)). Due to the larger cross-sections, we concentrate below on ionization to the

$\text{Ne}^{2+}(2p^4 3P)$ state, which proceeds in the LS coupling approximation via the three channels (in the dipole approximation):



In the Cooper–Zare model, the amplitudes of the two last (Ed) channels are proportional; the 2D amplitude is $\sqrt{3}$ times greater than the 2P amplitude.

An example of the corresponding analysis is presented in Fig. 4 for the photon energy 53 eV. In contrast to all previous complete experiments, we determined the ratio R_2 and the relative phase φ for the ionic photoionization, and simultaneously determined the ratio R_1 for the first ionization step.

The parameters β_k^ν can be expressed as functions f_k^ν of the parameters R_1 , $R_2 \cos \varphi$ and $R_2 \sin \varphi$ (see Supplementary Information). Using the experimental data, we define volumes in the $\{R_1, R_2 \cos \varphi, R_2 \sin \varphi\}$ space, composed of the points fulfilling the relations:

$$\beta_k^\nu - \Delta\beta_k^\nu < f_k^\nu(R_1, R_2 \cos \varphi, R_2 \sin \varphi) < \beta_k^\nu + \Delta\beta_k^\nu \quad (3)$$

where $\Delta\beta_k^\nu$ is the experimental error on the measured value β_k^ν . The volumes for the experimental values for $\beta_2^L(3P)$, $\beta_2^C(3P)$ and $\beta_4^L(3P)$ are shown in Fig. 4a–c, respectively. The intersection of the

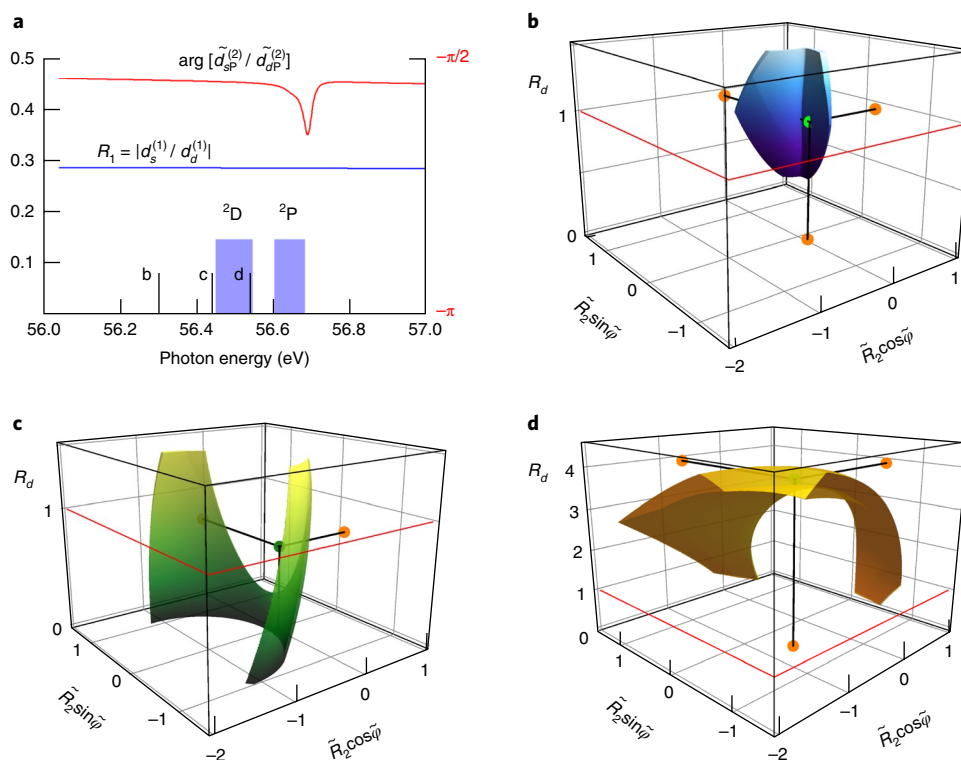


Fig. 5 | Complete experiment on photoionization of $\text{Ne}^+ 2p^5 2P$ to the $\text{Ne}^+ 2p^4 3P$ state at the photon energies close to the region of autoionizing resonances. **a**, Calculated (see Supplementary equation (6)) relative phase between the amplitudes $\tilde{d}_{sp}^{(2)}$ and $\tilde{d}_{dp}^{(2)}$ (right scale) and absolute ratio of the first-step amplitudes $\tilde{d}_s^{(1)}/\tilde{d}_d^{(1)}$ (left scale) as a function of the photon energy in the region of the $\text{Ne}^+ 2s2p^5 3p \ ^2D$ and 2P autoionizing states. The proposed method of extracting parameters \tilde{R}_2 , R_d and $\tilde{\varphi}$ works in the region where both curves are horizontal straight lines. The positions of the autoionizing states 2D and 2P together with their natural widths are indicated by the blue bands. **b–d**, 3D plots: allowed parameter space for the different photon energies indicated in **a**. The green dot is the result of the theoretical simulations in the three-parameter space, and the orange dots are their projections on the two-parameter spaces for better visualization. Note the different vertical scales between panels **b–d**.

three volumes is presented in Fig. 4d, together with the corresponding two-dimensional projections, and it represents the collection of points compatible with the experimental results. The simulation (green point in Fig. 4d, and corresponding yellow projections) is well within this allowed volume, confirming the validity of our physical model. The allowed values for R_1 determine the polarization of the intermediate ionic state (see Supplementary equations (8) and (9)).

Reconstruction in the presence of autoionizing states

When the photon energy approaches the region of the $\text{Ne}^+ 2s2p^5 3p \ ^2D$ and 2P autoionizing states, our method can be used in this resonant region as well, under the assumption that the presence of the autoionizing state $\text{Ne}^+ 2s2p^5 3p \ ^2P$ as the intermediate state in the reaction (2) resonantly modifies only the two amplitudes in the 2P channels, $\tilde{d}_{sp}^{(2)}$ and $\tilde{d}_{dp}^{(2)}$. Below we mark these resonance-modified amplitudes by a tilde (\sim). These two amplitudes, although both demonstrating a resonance behaviour (see Supplementary equation (6)), present a constant ratio and their relative phase is constant except in a very narrow range of energies close to the resonance, as shown in Fig. 5a. When crossing the resonance they quickly rotate almost simultaneously in the complex plane. Naturally, the 2D resonance does not influence their relative phase. Furthermore, the value of R_1 depends smoothly on the photon energy and its value outside the resonance region can be used. As a result, in the region of the 2D resonance, the absolute ratio of the amplitudes $\tilde{R}_2 = |\tilde{d}_{sp}^{(2)} / \tilde{d}_{dp}^{(2)}|$ and $R_d = |\tilde{d}_{dp}^{(2)} / \tilde{d}_{ad}^{(2)}|$ and the relative phase $\tilde{\varphi} = \arg(\tilde{d}_{sp}^{(2)} / \tilde{d}_{ad}^{(2)})$ can be taken as the parameters to be extracted in the complete experiment, assuming that the absolute ratio R_1 and the relative phase

$\arg[\tilde{d}_{sp}^{(2)} / \tilde{d}_{dp}^{(2)}]$ are fixed at their non-resonant values. Figure 5 illustrates the procedure in the presence of the autoionizing states, presenting the evolution of the allowed parameter space when the photon energy is in the resonance region. Far from the resonances, the ‘resonant’ (Fig. 5b) and ‘non-resonant’ (Fig. 4d) versions of the complete experiment converge (see Supplementary Information for a detailed discussion) as a consequence of the Cooper–Zare model: $\tilde{R}_2 \rightarrow R_2$, $R_d \rightarrow 1$, $\tilde{\varphi} \rightarrow \varphi$. Near the 2D resonance (Fig. 5c), the 2D channel becomes stronger, R_d decreases and the parameter space is confined to regions near the plane $R_d = 0$. When approaching the 2P resonance (Fig. 5d) the 2D and 2P amplitudes decrease and increase, respectively, the parameter space is elongated parallel to the R_d axis and the variation of the relative phase $\tilde{\varphi}$ starts; the last of these leads to a twisting of the allowed parameter space around the R_d axis. Further evolution of the parameter space is not shown because the model does not work adequately outside the region shown (see red curve in Fig. 5a).

Representation of bound and outgoing electrons

The extracted amplitudes determine, within our model of photoionization, any observable quantity after the reaction. As an example, Fig. 6 shows the spatial electron densities of the residual ions (Fig. 6a,b,g,h) and of the photoelectrons (Fig. 6d–f,j–l) after the first (Fig. 6a,d,g,j) and second (Fig. 6b,e,f,h,k,l) ionization steps. The amplitudes were taken from theoretical simulations (orange symbols in Fig. 5b,c), which are within the allowed amplitude space derived from our experiment. Figure 6c,i shows sections of the electronic densities of the residual ions Ne^{2+} for the off- (left-hand side) and on-resonance (right-hand side) cases. Deviations from the spherical symmetry (alignment) are clearly seen. In the resonance region the alignment

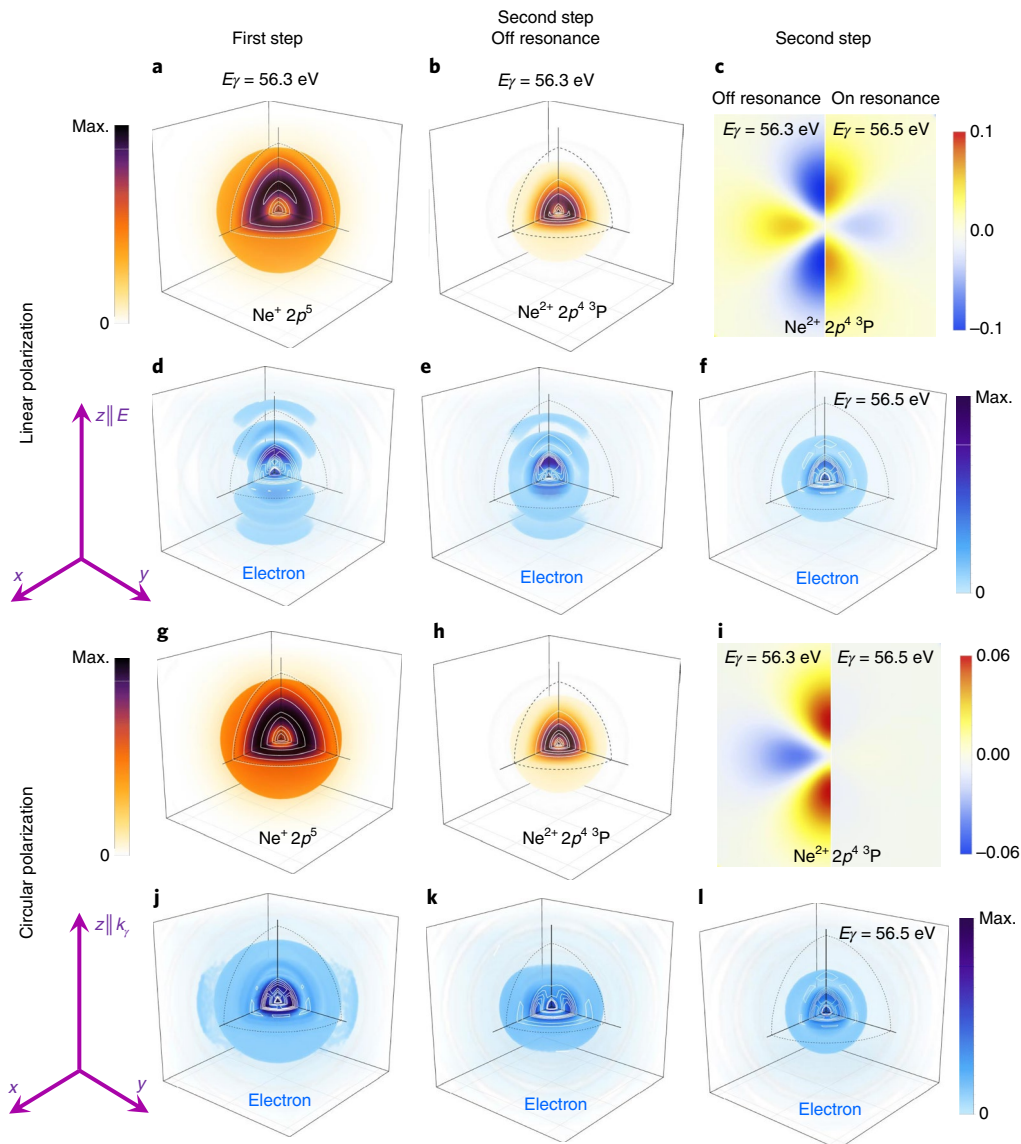


Fig. 6 | Reconstruction of bound and unbound electronic density distributions. **a,d,g,j**, Spatial electron density of the residual ion $\text{Ne}^+(2p^5 2P)$ (**a,g**) and of the scattering states of the corresponding photoelectron (**d,j**). **b,e,h,k**, Spatial electron density of the residual ion $\text{Ne}^{2+}(2p^4 3P)$ (**b,h**) and of the scattering states of the corresponding photoelectron (**e,k**) far from the autoionizing resonance. **f,l**, The photoelectron in the resonance region. **c,i**, Sections of the electron density of the residual ion $\text{Ne}^{2+}(2p^4 3P)$ (see the second term in Supplementary equation (13)) for the off-resonance (left half) and on-resonance (right half) cases. The dashed black lines indicate the radius of 5 a.u. (linear scale). The directions of the z axis along the electric field (linear polarization; two upper rows) and the propagation direction (circular polarization; two lower rows) of the FEL pulses are indicated. The three axes for **a,b,d-h,j-l** and **c,i** extend from -6.5 and $+6.5$ a.u., and from -3.25 to $+3.25$ a.u., respectively. 1 a.u. = 0.0529 nm is the Bohr radius.

is modified significantly and even changes sign due to enhancement of the contribution from the 2D channel. Note the practically isotropic Ne^{2+} ion produced by circularly polarized FEL light at resonance (Fig. 6i, right-hand side). The photoelectron cloud changes drastically as well (Fig. 6e,f,k,l) with changes of the photon energy by only 0.2 eV in the region of the autoionizing state. The clouds of photoelectrons produced in the first and in the second ionization steps differ strongly, reflecting different amplitude ratios and relative phases of the outgoing s and d partial electron waves. We have verified that the electronic distributions do not significantly change considering the amplitudes from any other point within the allowed parameter space.

Conclusions

We have shown that the use of VUV–XUV FELs with variable polarization enables the complete reconstruction of the bound and

unbound components of the electronic wavepackets created in the sequential two-photon double-ionization process. The complete characterization of multiple photoionization in noble gases is an important step towards an exhaustive description of nonlinear interaction under intense XUV fields. These investigations are needed to benchmark with experimental data the theoretical models^{33,35,44}. At the same time, the characterization of the interaction of ions with ultraviolet and XUV radiation is also important in astrophysics for understanding the dynamics occurring in plasma environments with temperatures between 10^3 and 10^6 K⁴⁵.

Online content

Any methods, additional references, Nature Research reporting summaries, source data, statements of data availability and associated accession codes are available at <https://doi.org/10.1038/s41567-018-0340-4>.

Received: 10 January 2018; Accepted: 9 October 2018;
Published online: 12 November 2018

References

- Böhme, D. K. Multiply-charged ions and interstellar chemistry. *Phys. Chem. Chem. Phys.* **13**, 18253–18263 (2011).
- Thissen, R. et al. Doubly-charged ions in the planetary ionosphere: a review. *Phys. Chem. Chem. Phys.* **13**, 18264–18287 (2011).
- Gillaspy, J. D., Pomeroy, J. M., Perrella, A. C. & Grube, H. The potential of highly charged ions: possible future applications. *J. Phys. Conf. Ser.* **58**, 451–456 (2007).
- McNeil, B. W. J. & Thompson, N. R. X-ray free-electron lasers. *Nat. Photon.* **4**, 814–821 (2010).
- Wabnitz, H. et al. Multiple ionisation of atom clusters by intense soft X-rays from a free-electron laser. *Nature* **420**, 482–485 (2002).
- Young, L. et al. Femtosecond electronic response of atoms to ultra-intense X-rays. *Nature* **466**, 56–61 (2010).
- Kollath, K. J. Theory for laser photoionisation of excited atoms: $n^2 P_{1/2,3/2}$ states of Cs. *J. Phys. B* **13**, 2901–2919 (1980).
- Becker, U. Complete photoionisation experiments. *J. Electr. Spectrosc. Relat. Phenom.* **96**, 105–115 (1998).
- Bederson, B. The ‘perfect’ scattering experiment. I. *Comm. Atom. Mol. Phys.* **1**, 41–44 (1969).
- Kleinpoppen, H. Analysis of scattering amplitudes in polarized-electron-atom collisions. I. Elastic scattering on one-electron atoms and the excitation process $^2S_{1/2} \rightarrow ^2P_{1/2,3/2}$. *Phys. Rev. A* **3**, 2015–2027 (1971).
- Duncanson, J. A. Jr., Strand, M. P., Lindgård, A. & Berry, R. S. Angular distributions of electrons from resonant two-photon ionization of sodium. *Phys. Rev. Lett.* **37**, 987–990 (1976).
- Cherepkov, N. A. Spin polarization of photoelectrons ejected from unpolarized atoms. *J. Phys. B* **12**, 1279–1296 (1979).
- Heinzmann, U. Experimental determination of the phase differences of continuum wavefunctions describing the photoionisation process of xenon atoms: I. Measurements of the spin polarisations of photoelectrons and their comparison with theoretical results. *J. Phys. B* **13**, 4353–4366 (1980).
- Heinzmann, U. Experimental determination of the phase differences of continuum wavefunctions describing the photoionisation process of xenon atoms: II. Evaluation of the matrix elements and the phase differences and their comparison with data in the discrete spectral range in application of the multichannel quantum defect theory. *J. Phys. B* **13**, 4367–4381 (1980).
- Kessler, J. The ‘perfect’ photoionization experiment. *Comm. Atom. Mol. Phys.* **10**, 47–55 (1981).
- Reid, K. L., Leahy, D. H. & Zare, R. N. Complete description of molecular photoionization from circular dichroism of rotationally resolved photoelectron angular distributions. *Phys. Rev. Lett.* **68**, 3527–3530 (1992).
- Cherepkov, N. A. et al. K-shell photoionization of CO: II. Determination of dipole matrix elements and phase differences. *J. Phys. B* **33**, 4213–4236 (2000).
- Geßner, O. et al. $4\sigma^{-1}$ inner valence photoionization dynamics of NO derived from photoelectron-photoion angular correlations. *Phys. Rev. Lett.* **88**, 193002 (2002).
- Kabachnik, N. M. & Sazhina, I. P. On the problem of a complete experimental characterisation of Auger decay. *J. Phys. B* **23**, L353–L357 (1990).
- Grum-Grzhimailo, A. N., Dorn, A. & Mehlhorn, W. On complete experiments for Auger decay. *Comm. Atom. Mol. Phys. Comm. Mod. Phys. D* **1**, 29–39 (1999).
- West, J. B., Ross, K. J., Ueda, K. & Beyer, H. J. Angular correlation measurement between the photo-excited autoionized electron and subsequent polarized fluorescent photon at an autoionization resonance of Sr. *J. Phys. B* **31**, L647–L654 (1998).
- Hergenhahn, U. et al. Dynamically induced spin polarization of resonant Auger electrons. *Phys. Rev. Lett.* **82**, 5020–5023 (1999).
- Becker, U. & Crowe, A. (eds) *Complete Scattering Experiments* (Kluwer Academic/Plenum, New York, 2001).
- Kleinpoppen, H., Lohmann, B. & Grum-Grzhimailo, A. N. *Perfect/Complete Scattering Experiments* (Springer, Berlin, 2013).
- Allaria, E. et al. Control of the polarization of a vacuum-ultraviolet, high-gain, free-electron laser. *Phys. Rev. X* **4**, 041040 (2014).
- Flügge, S., Mehlhorn, W. & Schmidt, V. Angular distribution of Auger electrons following photoionization. *Phys. Rev. Lett.* **29**, 7–9 (1972).
- Jacobs, V. L. Theory of atomic photoionization measurements. *J. Phys. B* **5**, 2257–2271 (1972).
- Caldwell, C. D. & Zare, R. N. Alignment of Cd atoms by photoionization. *Phys. Rev. A* **16**, 255–262 (1977).
- Greene, C. H. & Zare, R. N. Photofragment alignment and orientation. *Ann. Rev. Phys. Chem.* **33**, 119–150 (1982).
- Allaria, E. et al. Highly coherent and stable pulses from the FERMI seeded free-electron laser in the extreme ultraviolet. *Nat. Photon.* **6**, 699–704 (2012).
- Lyamayev, V. et al. A modular end-station for atomic, molecular, and cluster science at the low density matter beamline of FERMI@Elettra. *J. Phys. B* **46**, 164007 (2013).
- Covington, A. M. et al. Photoionization of Ne⁺ using synchrotron radiation. *Phys. Rev. A* **66**, 062710 (2002).
- Fritzsche, S., Grum-Grzhimailo, A. N., Gryzlova, E. V. & Kabachnik, N. M. Angular distributions and angular correlations in sequential two-photon double ionization of atoms. *J. Phys. B* **41**, 165601 (2008).
- Peshkin, M. in *Advances in Chemical Physics* Vol. 18 (eds Prigogine, I. & Rice, S. A.) 1–14 (Interscience, New York, 2007).
- Gryzlova, E. V., Grum-Grzhimailo, A. N., Fritzsche, S. & Kabachnik, N. M. Angular correlations between two electrons emitted in the sequential two-photon double ionization of atoms. *J. Phys. B* **43**, 225602 (2010).
- Nikolopoulos, L. A. A. Time-dependent theory of angular correlations in sequential double ionization. *Phys. Rev. Lett.* **111**, 093001 (2013).
- Kaneyasu, T. et al. Autoionization of the Ne⁺ Rydberg states formed via valence photoemission. *J. Phys. B* **40**, 4047–4060 (2007).
- Faye, M. et al. Modified orbital atomic theory calculations of high lying Rydberg series in the photoionization spectra of Ne⁺. *Chin. J. Phys.* **53**, 100401 (2015).
- Edwards, A. K. & Roud, M. E. Excitation of auto-ionizing levels in neon by ion impact. *Phys. Rev.* **170**, 140–144 (1968).
- Morgenstern, R., Niehaus, A. & Zimmermann, G. Autoionizing states formed by electron capture in collisions of multiply charged Ne ions with He, H₂ and Xe. *J. Phys. B* **13**, 4811–4831 (1980).
- Braune, M. et al. Electron angular distributions of noble gases in sequential two-photon double ionization. *J. Mod. Optics* **63**, 324–333 (2016).
- Cooper, J. & Zare, R. N. Angular distribution of photoelectrons. *J. Chem. Phys.* **48**, 942–943 (1968).
- Cooper, J. W. & Zare, R. N. in *Lectures in Theoretical Physics* Vol XI-C (eds Geltman, S. et al.) 317 (Gordon and Breach, New York, 1969).
- Grum-Grzhimailo, A. N., Gryzlova, E. V., Fritzsche, S. & Kabachnik, N. M. Photoelectron angular distributions and correlations in sequential double and triple atomic ionization by free electron lasers. *J. Mod. Optics* **63**, 334–357 (2016).
- Gómez de Castro, A. I. & Wamsteker, W. (eds) *Fundamental Questions in Astrophysics: Guidelines for Future UV Observatories* (Springer, Dordrecht, 2006).

Acknowledgements

Financial support by the Italian Ministry of Research (project FIRB no. RBID08CRXK) is gratefully acknowledged. This project has also received funding from the European Union's Horizon 2020 research and innovation programme under the Marie Skłodowska-Curie grant agreement no. 641789 MEDEA. D.F. and M.N. acknowledge support from the European Research Council Starting Research Grant UDYNI (grant agreement no. 307964). K.U. acknowledges support by the X-ray Free Electron Laser Utilization Research Project and the X-ray Free Electron Laser Priority Strategy Program of the Ministry of Education, Culture, Sports, Science and Technology of Japan (MEXT), by the Cooperative Research Program of ‘Network Joint Research Center for Materials and Devices: Dynamic Alliance for Open Innovation Bridging Human, Environment and Materials’, by the bilateral project CNR-JSPS ‘Ultrafast science with extreme ultraviolet Free Electron Lasers’ and by the IMRAM project for the international co-operation. M.M. acknowledges support by the Deutsche Forschungsgemeinschaft (DFG) under grant no. SFB 925.

Author contributions

K.U., G.S. and A.N.G.-G. conceived the present study. M.R., D.F., M.N., K.U., F.F., E.S., Y.O., M.M., O.P., P.F., K.C.P., C.C. and G.S. conducted the experiment. P.A.C. analysed the experimental data. A.D. contributed to the development of the analysis programmes. E.V.G., S.M.B. and A.N.G.-G. developed the theoretical background and performed the numerical simulations. E.V.G., A.N.G.-G. and G.S. drafted the manuscript. All authors discussed the experimental results and the final version of the manuscript.

Competing interests

The authors declare no competing interests.

Additional information

Supplementary information is available for this paper at <https://doi.org/10.1038/s41567-018-0340-4>.

Reprints and permissions information is available at www.nature.com/reprints.

Correspondence and requests for materials should be addressed to A.N.G. or G.S.

Publisher's note: Springer Nature remains neutral with regard to jurisdictional claims in published maps and institutional affiliations.

© The Author(s), under exclusive licence to Springer Nature Limited 2018

Methods

The experiment was performed at the Low Density Matter beamline at the seeded XUV-FEL, FERMI, which offers fine tunability and narrow bandwidth (0.15% full-width at half-maximum (FWHM), 80–96 meV measured in the 56.2–56.7 eV range). The photon energy of the FEL was tuned via the seed laser and the undulator gaps. The step size was set to 0.5 eV in the spectral range 40–60 eV (long scans) and 20 meV between 55.5 and 56.8 eV (fine scans). The FEL pulse duration was estimated to be about 50 fs FWHM with a Gaussian spatial profile of 22 μm diameter (FWHM) measured at the focus³⁰. The laser pulse energy on target ($10 \pm 3 \mu\text{J}$ for linear and $13 \pm 3 \mu\text{J}$ for circular polarization) was calculated from the value measured shot-by-shot by the ionization yield in a pulse energy monitor and took into account the calculated nominal reflectivity (65%) of the optical elements in the beam transport system³⁰. With these parameters, the calculated intensity, averaged over the spot size and the pulse duration, was $I = 1.2 \times 10^{13} \text{ W cm}^{-2}$ for linear polarization. VMIS images were obtained by integrating the single-shot acquisitions over 4,000 consecutive laser shots with background subtraction.

In the energy region of the second ionization peaks, the energy resolution of the VMIS is $\sim 500 \text{ meV}$. Thus, the three substates $^3P_{0,1,2}$ of the second ionization step, separated by 30 and 80 meV, and the spin-orbit splitting of 97 meV of the intermediate state doublet $\text{Ne}^+ 2p^5 2P_{1/2,3/2}$ cannot be experimentally resolved (see Fig. 1).

The VMIS projects the three-dimensional photoelectron distribution on the two-dimensional surface of the detector. If the distribution has an axis of symmetry in the plane of the detector, the original angular distribution can be retrieved from the two-dimensional projection by means of an inverse-Abel transform. The pBasex software was used for the inversion. Spatial variations of the detector sensitivity and elliptical distortions were corrected before inversion. The error bars for β_2^v and β_4^v were calculated as the standard deviation of the data points for the 2s peak, whose betas do not depend on the photon energy ($\beta_2^L = 2$ and $\beta_4^L = 0$ for linear polarization and $\beta_2^C = -1$ and $\beta_4^C = 0$ for circular polarization). The error bars were extended to the parameters of the other photoelectron peaks, as they show similar features on the VMIS images. The same approach was adopted for the relative error on the peak intensity, which does not depend on the photon energy for the 2s peak in the narrow spectral region of the autoionizing states. This procedure was cross-checked by comparing the values retrieved for data points acquired in the same experimental conditions and in different experimental runs. The energies of the two photoionization steps are listed in Supplementary Table 2.

In the intermediate-coupling multiconfiguration Hartree–Fock calculations, we obtained the wavefunctions by mixing configurations with single and double replacements of the electrons with the principal quantum numbers $n=2$ and $n=3$ by $3d$, $4s$ and $4p$ electrons of the basic configurations $1s^2 2s^2 2p^5$ for the ground state of Ne^+ , $1s^2 2s 2p^3 3p$ for the autoionizing states of Ne^+ and $1s^2 2s^2 2p^4$ for the ground state of Ne^{2+} . The calculated energies of autoionizing states were scaled to the term-averaged position of the $2s 2p^3 3p$ 3D state with the experimental energy of 56.53 eV with respect to the $\text{Ne}^+ 2p^5 2P_{3/2}$ state⁴⁰. These energies are listed in Supplementary Table 3.

The Fano profile indices of the autoionizing states are similar for the fine-structure levels: $q_{2p} = -3.5$, $q_{2p} = -4.5$ and $q_{2s} = 6$. The last one is rather sensitive and varies within the interval 5–10 for different choices of the orbitals. In the present experiment, the $2s 2p^3 3p$ 2S state was outside the region of our interest and affects only the high-energy part of the spectrum. We used the statistical tensor formalism⁴⁷ and the procedure proposed in refs^{48,49} to express the parameters $\beta_{2,4}^v$ in terms of matrix elements in the region of the autoionizing resonances, as described in the Supplementary Information.

Having the full set of the dipole amplitudes $D_{i \rightarrow f}$ of transitions from initial (i) to final (f) states, any observable Q in the final state can be found according to the quantum-mechanical prescription

$$\langle Q \rangle = \text{Tr}(\rho Q) = \sum_{ff'ii'} \langle \xi_f | \rho_0 | \xi_i \rangle \langle \chi_{f'} | Q | \chi_f \rangle D_{i \rightarrow f} D_{i' \rightarrow f'}^* \quad (4)$$

where ρ (ρ_0) is the density matrix in the final (initial) state of the atom or ion, and $|\xi_f\rangle$ ($|\chi_f\rangle$) is a basis set for the initial (final) states. In the case when Q describes a subsystem (residual ion or photoelectron), the corresponding reduced density

matrix should be taken. The electron density ('electron cloud') of the residual ion is obtained from the electron density operator $Q = \sum_n \delta(\mathbf{r} - \mathbf{r}_n)$, where \mathbf{r}_n is the coordinate of the n th electron and the summation is over all electrons except one (photoelectron). For example, for the density of the electron cloud of the residual ion $\text{Ne}^+(2p^5 2P)$

$$N(\mathbf{r}) = C \sum_{lmm_s} \sum_{M'M_S} \langle {}^2P_{MM_S}, lmm_s | D_\nu | 0 \rangle \langle {}^2P_{M'M_S}, lmm_s | D_\nu | 0 \rangle^* \times \langle {}^2P_{MM_S}, lmm_s | \sum_{n=1}^9 \delta(\mathbf{r} - \mathbf{r}_n) | {}^2P_{M'M_S}, lmm_s \rangle \quad (5)$$

where $D_\nu = \sum_{n=1}^{10} (r_\nu)_n$ is the spherical component of the dipole, $\nu=0$ for linearly polarized light and $\nu=\pm 1$ is the helicity for circularly polarized light, and $M(M')$ and M_S are the projection of the orbital and spin momentum of the ion, respectively; m and m_s are the corresponding projections of the photoelectron and C is a normalization constant. We introduced short notations $|0\rangle$ for the ground state $\text{Ne}(2p^6 1S)$ and $|{}^2P_{MM_S}\rangle$ for the state $\text{Ne}^+(2p^5 2P_{MM_S})$. One can obtain after some algebra from equation (5) a similar equation for the electron cloud of $\text{Ne}^{2+}(2p^4 2S^{\pm 1} L_f)$, $N(\mathbf{r}) = N_{2p}(\mathbf{r}) + N_{\text{core}}(\mathbf{r})$, where $N_{\text{core}}(\mathbf{r})$ is the electron cloud of the inner 1s and 2s shells and

$$N_{2p}(\mathbf{r}) \equiv N_L^{(j)}(\mathbf{r}) = C^{(j)} |R_{2p}^{(j)}(r)|^2 (1 + \alpha_2^{(j)} A_{20}^{(j)} P_2(\cos\theta)) \quad (6)$$

is the cloud of the 2p shell. Here j indicates either $\text{Ne}^+(2p^5)$ ($j=1$) or $\text{Ne}^{2+}(2p^4)$ ($j=2$) residual ion, $A_{20}^{(j)}$ is the ion alignment, $R_{2p}^{(j)}(r)$ is the 2p radial wavefunction and

$$\alpha_2^{(j)} = \sqrt{6(2L_f + 1)} \sum_{L'S'} (G_{S'L'}^{S_L L_f})^2 \begin{Bmatrix} 1 & 1 & 2 \\ L_f & L_f & L' \end{Bmatrix} \quad (7)$$

where $G_{S'L'}^{S_L L_f}$ is the coefficient of fractional parentage⁵⁰: $G_{S'L'}^{S_L L_f(1)} = (p^4 L' S | p^5 2P)$ (that is, $L_f=1$, $S_f=\frac{1}{2}$ and terms $L'S'$ run over 3P , 1D and 1S); $G_{S'L'}^{S_L L_f(2)} = (p^3 L' S | p^4 L_f S_f)$ (that is, terms $L_f S_f$ run over 3P , 1D and 1S and terms $L'S'$ run over 3P , 3D and 3S).

To obtain the photoelectron cloud, we take $Q = \delta(\mathbf{r} - \mathbf{r}_{\text{ph}})$, where \mathbf{r}_{ph} is the coordinate of the photoelectron. Its spatial density, shown in Fig. 6d–f, is described by the same formula (equation (1)) as the PAD, where the angle θ characterizes now the direction of the radius vector \mathbf{r} , and not the direction of the electron propagation, while the parameters β_2^v and β_4^v are given by Supplementary equations (1)–(5) with the substitution $D_{i \rightarrow f}^{(2)} \rightarrow D_{i \rightarrow f}^{(2)} R_{E, L_2}(r)$, where $R_{E, L_2}(r)$ is the radial function of the photoelectron with kinetic energy E and orbital angular momentum L_2 , calculated for the total orbital momentum L_2 of the system (ion + photoelectron).

Data availability

The data that support the plots within this paper and other findings of this study are available from the corresponding author upon reasonable request.

References

- Svetina, C. et al. The Low Density Matter (LDM) beamline at FERMI: optical layout and first commissioning. *J. Synchrotron Radiat.* **22**, 538–543 (2015).
- Balashov, V., Grum-Grzhimailo, A. & Kabachnik, N. *Polarization and Correlation Phenomena in Atomic Collisions: A Practical Theory Course* (Plenum, New York, 2000).
- Kabachnik, N. & Sazhina, I. Angular distribution and polarization of photoelectrons in the region of resonances. *J. Phys. B* **9**, 1681–1697 (1976).
- Baier, S., Grum-Grzhimailo, A. & Kabachnik, N. Angular distribution of photoelectrons in resonant photoionization of polarized atoms. *J. Phys. B* **27**, 3363–3388 (1994).
- Cowan, R. D. *The Theory of Atomic Structure and Spectra* (Univ. California Press, Berkeley, 1981).